Imaging Performance of A-PET: A Small Animal PET Camera

Suleman Surti*, *Member, IEEE*, Joel S. Karp, *Senior Member, IEEE*, Amy E. Perkins, *Member, IEEE*, Chris A. Cardi, Margaret E. Daube-Witherspoon, *Member, IEEE*, Austin Kuhn, and Gerd Muehllehner, *Fellow, IEEE*

Abstract—The evolution of positron emission tomography (PET) imaging for small animals has led to the development of dedicated PET scanner designs with high resolution and sensitivity. The animal PET scanner achieves these goals for imaging small animals such as mice and rats. The scanner uses a pixelated Anger-logic detector for discriminating $2 \times 2 \times 10$ mm^3 crystals with 19-mm-diameter photomultiplier tubes. With a 19.7-cm ring diameter, the scanner has an axial length of 11.9 cm and operates exclusively in three-dimensional imaging mode, leading to very high sensitivity. Measurements show that the scanner design achieves a spatial resolution of 1.9 mm at the center of the field-of-view. Initially designed with gadolinium orthosilicate but changed to lutetium- yttrium orthosilicate, the scanner now achieves a sensitivity of 3.6% for a point source at the center of the field-of-view with an energy window of 250–665 keV. Iterative image reconstruction, together with accurate data corrections for scatter, random, and attenuation, are incorporated to achieve high-quality images and quantitative data. These results are demonstrated through our contrast recovery measurements as well as sample animal studies.

Index Terms—Anger detector with gadolinium orthosilicate (GSO) or lutetium-yttrium orthosilicate (LYSO), animal positron emission tomography (PET) imaging, high resolution, high sensitivity.

I. INTRODUCTION

FOR THE last ten years, significant efforts in the development of high-resolution animal PET scanners [1]–[12] have led to an increased use and acceptance of *in vivo* molecular imaging techniques in biological laboratories. *In vivo* molecular imaging has an advantage over other traditional radionuclide techniques by allowing the use of the same animal to perform longitudinal studies over long periods of time and the acquisition of statistically relevant and quantitative data. Molecular imaging of small laboratory animals, such as mice and rats, is a vital tool in the study of disease and there are many potential

uses of positron emission tomography (PET) imaging in small animals [13]–[20]. Mouse models of human diseases, such as cancer, Parkinson's disease, and Alzheimer's, are providing important clues to the causes, diagnosis, and treatment of these, and many other, disorders. Numerous studies have been presented showing small-animal PET imaging in a variety of applications, such as imaging neuronal activation and plasticity in the rat brain [21], imaging gene expression [22]–[25], and imaging receptor binding and occupancy [26], [27].

In this paper, we describe and evaluate the performance of an animal PET scanner (A-PET) designed to achieve good spatial resolution (~2 mm) and high sensitivity in a simplified design. The A-PET has a very long axial field-of-view (almost 12 cm) in order to perform whole-body biodistribution studies of animals such as mice and rats in one to three bed positions. The relatively large diameter of the scanner (19.7 cm) provides the capability to image large animals such as cat or primate heads, although the software currently limits the transverse field-of-view (FOV) to 12.8 cm. Originally, the scanner incorporated gadolinium orthosilicate (GSO) scintillators (Hitachi Chemical Co., Ltd., Ibaraki, Japan) in an optically continuous, pixelated Anger-logic detector. The system was tested to validate the design, and performance measurements were taken, while several imaging protocols were initiated. These initial results are summarized here and described also in [28]. This design has been translated into a commercial system by Philips Medical Systems called Mosaic. After six months of use, we changed the system by replacing the GSO scintillator with lutetium-yttrium orthosilicate (LYSO) crystals (Photonic Materials Ltd., Bellshill, Scotland, U.K.), which have higher stopping power and higher light output. While in recent years, other researchers have focused on developing PET scanners with spatial resolution approaching 1–1.5 mm [5], [6], [8], [11], our primary design goal was to emphasize high sensitivity with a large imaging field-of-view and with a small compromise in spatial resolution. This is because for certain high-affinity radio-ligands in brain receptor imaging, the specific activity is low enough that injection of high activity levels can lead to a reduction in the specific binding of the radio-ligand [18], [19]. As a result, for many research areas involving small-animal imaging, the scanner sensitivity becomes just as important as high spatial resolution.

The detectors used for dedicated animal PET scanners span a wide range and represent varying degrees of complexity. The A-PET scanner uses a pixelated Anger-logic detector [29] with conventional 19-mm-diameter photomultiplier tubes (PMTs) leading to a high ratio of crystals-per-PMT (encoding ratio) of 58. In comparison, some other scanners utilize a one-to-one coupling of single crystals to an avalanche photodiode [1], [30] as in the Sherbrooke and Munich Avalanche Diode (MAD) PET

[9], [31] designs. Other animal scanner detectors range from the standard [12] and quadrant-sharing block design [11] to optical fibers coupled to a PMT [2], [4]–[7] and discrete crystals directly coupled to a position-sensitive PMT [10]. In general, as the detector design shifts from the use of a conventional PMT, the crystals-per-PMT channel encoding ratio generally decreases, which leads to increased complexity in the readout electronics. Besides the traditional inorganic scintillator-based animal PET scanners, there is also a commercially available animal scanner using an array of high-density avalanche chambers [8] as the photon detector.

Keeping the detector, scanner, and electronics designs the same, but using two different scintillators, we measured the performance of the GSO and LYSO scanners in small-animal imaging situations. In addition to evaluating the physical characteristics such as spatial resolution, sensitivity, and count-rate behavior, we also demonstrate very good imaging performance with animal studies on this scanner.

II. SCANNER DESIGN

A. Detector and Electronics

The scanner design utilizes a single annular lightguide 1.2 cm thick (with 0.5-cm-deep slots), coupled with 14 456 crystals (each measuring $2 \times 2 \times 10$ mm^3) in an optically continuous, pixelated Anger-logic design. Signal readout is performed via an array of 288 19-mm-diameter PMTs. The 10-mm-long crystals were chosen as a tradeoff between scanner sensitivity and parallax error in a small ring diameter. The crystal pitch is 2.3 mm for a packing efficiency of 75%. The lightguide size results in a scanner diameter of 19.7 cm (reconstructed transverse field-of-view of 12.8 cm) with an axial length of 11.9 cm. This scanner is operated exclusively in the three-dimensional (3-D) volume imaging mode, leading to about a 55% coverage of the total solid angle (in singles) for a point source at the center of the scanner FOV. The design of this scanner represented a scaled-down version of a previously developed dedicated GSO-based brain scanner (G-PET) [32], which used $4 \times 4 \times 10$ mm^3 crystals. The crystal dimension of 4 mm, the axial FOV, and the diameter of G-PET were all reduced by a factor of two in designing the A-PET scanner. The original A-PET design also used GSO [28] crystals, but recently we replaced the GSO with LYSO crystals, which have the advantage of higher sensitivity and higher light output but the disadvantage of higher cost. There were several reasons for replacing the GSO with LYSO. LYSO was initially not available when this project started, while the availability of lutetium orthosilicate (LSO), which has almost identical scintillation properties to those of LYSO, was limited. Also, the recent development of LYSO has demonstrated the ability to achieve comparable light output uniformity and energy resolution to the GSO scintillator. In the discrete Anger-logic detector that we use in our scanner designs, the GSO crystal discrimination was very good for the 4-mm crystals originally used in the G-PET and the whole-body Allegro [33] (with 39-mm PMTs) but only fair for the 2-mm crystals (with 19-mm PMTs). The higher light output of LYSO leads to better crystal discrimination for the 2-mm crystals. Typical peak-to-valley ratios in a crystal flood image are 1.9 and 1.2 for the LYSO and GSO scanners, respectively. The increased stopping power of the LYSO also results in improved
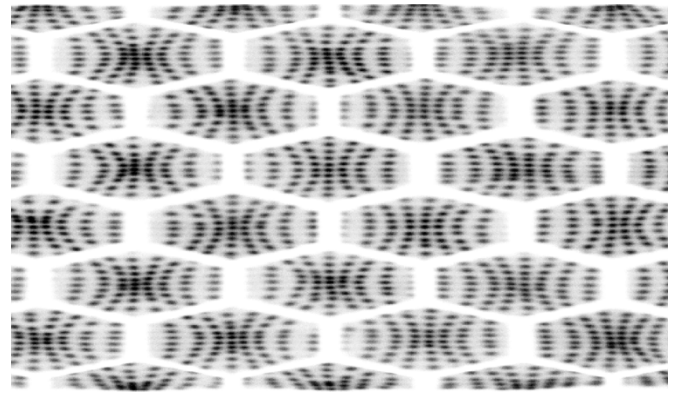

Fig. 1. Portion of the crystal flood from a 511 keV point source at the center of the LYSO scanner. Each hexagonal region shows the spatial distribution of counts collected in the crystals directly below a PMT, along with a clear separation of the individual crystals.

sensitivity over the GSO-based A-PET scanner. Finally, a manufacturing problem in the lightguide for the original GSO scanner required a replacement, and we took the opportunity to replace the crystals with LYSO.

The electronics architecture is derived from the original PENN PET system with multiple trigger channels across the whole scanner surface to minimize deadtime [34]–[36]. Additionally, only those events that form valid coincidences are integrated and subsequently processed in the electronics. Integration is performed by summing multiple signal samples obtained by flash (asynchronous) analog-to-digital converters running at 50 MHz. The coincidence timing window was set at 12 ns for GSO and reduced to 7 ns for LYSO due to its better timing resolution.

B. Data Calibrations, Corrections, and Reconstruction

Before the position of an interaction event is calculated, a PMT gain calibration is performed via a lookup table to account for variations in gain for individual PMTs. Position calculation is performed using local Anger logic over a cluster of seven PMTs, followed by binning of the calculated position into a physical crystal position on the scanner based on a lookup table. Also, in order to achieve a good system energy resolution and, thus, use a tight energy window for collected events, a position-based lookup table is used to scale the measured energy. This calibration accounts for possible variations in individual crystal light outputs, as well as the 20% (maximum) difference in collected light for crystals at the center of a PMT and those at the "triple point." The triple point is an area of the detector that is not directly below any PMT and arises due to the dead space between any three PMTs arranged in a hexagonal close-packed array. The default energy window was set to 385–665 keV, but we have investigated raising the lower value of the energy window in the LYSO scanner in order to better utilize the good system energy resolution of 17%. Fig. 1 shows the typical flood map obtained with the LYSO scanner which leads to a robust crystal identification procedure from a lookup table.

The collected data from the scanner are binned into a sinogram with 139 angles and 125 rays for every ring combination covering a 128-mm transverse FOV. Linear interpolation in the transverse direction is performed to rebin these data into a 256×192 sinogram for FOV of either 64 or 128 mm, up to

TABLE I
ABSOLUTE SENSITIVITY (%) FOR THE LYSO SCANNER MEASURED
WITH A ^{68}Ge POINT SOURCE FOR VARYING ENERGY WINDOWS

	250-665 keV	300-665 keV	350-665 keV	385-665 keV
Sensitivity (%)	3.6	3.1	2.7	2.5

TABLE II
ABSOLUTE SENSITIVITY (cps/kBq) MEASURED WITH A LINE SOURCE FOR
DEFAULT ENERGY WINDOW OF 385–665 keV

	A-PET (GSO)	A-PET (LYSO)
cps/kBq in 15 cm long line source	6.9	13.0
cps/kBq in the scanner FOV	8.7	16.3

TABLE III
ABSOLUTE SENSITIVITY (cps/kBq) FOR THE LYSO SCANNER MEASURED
WITH A LINE SOURCE FOR VARYING ENERGY WINDOWS

	cps/kBq in 15 cm long line source	cps/kBq inside the scanner FOV
250-665 keV	18.9	23.8
385-665 keV	13.0	16.3
410-665 keV	11.8	14.9
430-665 keV	10.4	13.0

15 tilts (out of plane angles) for an acceptance angle of $\pm 28°$, and 0.5- or 1-mm-thick slices.

Scatter correction can be performed by either a model-based single scatter simulation [37] or through a tail-fitting algorithm using a high-order polynomial fit. Random coincidences are estimated using a delayed coincidence window technique. These counts are either directly subtracted or averaged using the technique of Casey *et al.* [38] and then subtracted from the collected events.

Attenuation correction is performed by acquiring transmission scans in a singles mode using a 370 MBq (10 mCi) ^{137}Cs transmission source [39]. The transmission source can be placed both inside the scanner and outside it. Positioning the source outside the scanner permits easier access to both the source and the animal as well as imaging of larger animals. Transmission images are reconstructed using the ordered subsets estimation maximization algorithm for transmission data [40], adapted for the cone-beam geometry of the acquired data [41]. Routine image reconstruction is performed with a fast, fully 3-D iterative algorithm (3D-RAMLA) [42]–[44] into a 128×128 or 256×256 transverse image with cubic image voxels of dimensions either 1 and 0.5 mm, respectively.

III. SCANNER MEASUREMENTS AND RESULTS

A. Sensitivity

Absolute sensitivity was first measured with a 120 μCi ^{68}Ge point source placed at the center of the FOV. Data were collected for an energy window of 385–665 keV. Delayed coincidences were subtracted to remove the random coincidences arising from the ^{176}Lu background, and a branching ratio of 89% for ^{68}Ga was accounted for as well. The absolute sensitivity measured this way is 1.2% and 2.5% for the GSO and LYSO scanners, respectively. The measurements on the LYSO scanner were also repeated for different energy windows, and the results are summarized in Table I.

An absolute sensitivity measurement based on work described previously by Bailey *et al.* [45], [46] and recently adopted as a standard in the NEMA NU 2-2001 measurements for whole-body PET scanners [47] was also performed. The measurement was performed using a 15-cm-long ^{18}F line source at the center of the scanner, without and with four different metal sleeves representing varying amounts of attenuation. The measured count rate with each metal sleeve was corrected for activity decay and the natural logarithm of the results plotted as a function of sleeve thickness. Linear regression was employed to fit the data and obtain an extrapolated value for the absolute sensitivity of the scanner with no metal sleeves. The sensitivity measurement was performed using the standard energy window of 385–665 keV on both scanners. The results are shown in Table II for activity in the full length of the line source as well as normalized to activity within the scanner FOV. The measurements on the LYSO scanner were also repeated for varying energy windows, and the results are summarized in Table III.

B. Spatial Resolution

Spatial resolution measurements were performed using a point source of ^{18}F in a thin glass capillary tube with an inner diameter of 0.8 mm. The point source was placed at four to five different radial positions in the scanner and centered axially. The sinogram data were acquired in 15 tilt (out-of-plane) angles and reconstructed using the 3-D Fourier reprojection (3D-FRP) [48] algorithm, with an unapodized filter (ramp filter with a cutoff at the Nyquist frequency). The analytical 3D-FRP reconstruction is similar to Fourier rebinning [49] followed by filtered back-projection, except that it does not suffer from axial resolution degradation arising from the rebinning of a 3-D data set into two-dimensional. The images were reconstructed into a 256×256 transverse image for transverse FOV of 64 and 128 mm, resulting in cubic image voxels of dimension 0.25 mm for point source positions within 64 mm of the scanner center and 0.5 mm for positions beyond it. The full-width at half-maximum (FWHM) and full-width at tenth-maximum (FWTM) of the point spread functions were determined in all three directions by forming one-dimensional response functions through the peak of the distribution in the three orthogonal directions. The width of these profiles at right angles to the direction of measurement was $\sim$2 times the FWHM in those directions (wide profile) as required by the NEMA NU2-2001 standard [47], rather than a single pixel, in order to reduce measurement variability. The FWHM and FWTM were calculated by linear interpolation between adjacent pixels at one-half or one-tenth of an estimate of the maximum value of the response function. The spatial resolution analysis procedure follows that defined by the NEMA NU2-2001 standard for whole-body PET scanners, since the standards are yet to be defined for animal scanners. The results for the GSO and LYSO scanners are plotted in Fig. 2.

Near the center of the FOV, the transverse FWHM (FWTM) resolution for the LYSO scanner is 2.3 mm (4.8 mm), while the axial FWHM (FWTM) is 2.4 mm (5.5 mm). Similarly, near the center of the FOV, the transverse FWHM (FWTM) resolution for the GSO scanner is 2.3 mm (5.1 mm), while the axial FWHM (FWTM) is 3.1 mm (6.3 mm). For comparison, we also used profiles only one pixel wide (narrow profile) for analyzing the
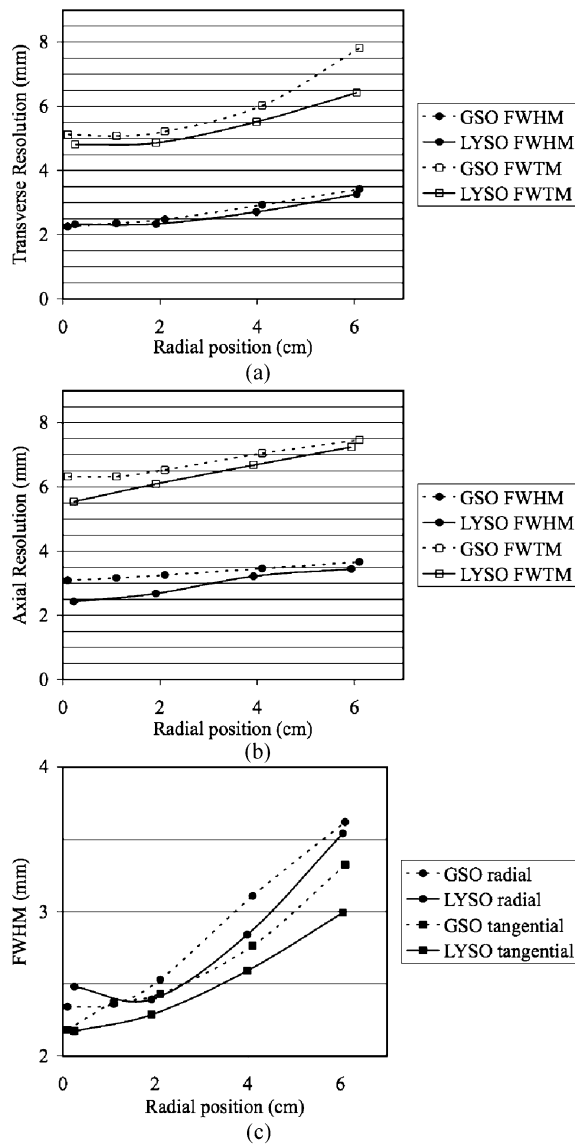
Fig. 2. (A) Transverse and (B) axial spatial resolution for the GSO and LYSO scanners. For the analysis, the profile widths were about twice the spatial resolution of the scanner (wide profile) as in NEMA NU2-2001 standards. In (C) the two components (radial and tangential) of the transverse FWHM are plotted separately for the GSO and LYSO scanners.

data from the LYSO scanner as some investigators report measurements this way. Our analysis with the narrow profiles shows that near the center of FOV, the transverse FWHM (FWTM) resolution is 1.9 mm (4.0 mm), while the axial FWHM (FWTM) is 2.4 mm (5.2 mm).

C. Scatter Fraction

To determine the scatter fraction $(Sc/(T + Sc))$, where Sc and T are the scatter and true counts at low count-rates), we used two cylindrical phantoms of sizes 6-cm diameter by 15-cm length (rat phantom, vol $= 424\,cm^3$) and 3-cm diameter by 7-cm length (mouse phantom, vol. $= 49\,cm^3$). For accurate measurement of the scatter and in keeping with the standards originally developed for the whole-body scanners (NEMA NU2-2001), we evaluated two solid cylindrical phantoms made out of polyethylene (specific gravity of 0.96 g/cc), which has attenuation

TABLE IV
COMPARISON OF SCATTER FRACTION CALCULATED IN MONTE CARLO SIMULATIONS FOR A RAT AND MOUSE PHANTOM WITH UNIFORM ACTIVITY DISTRIBUTION AND WITH A LINE SOURCE PLACED AT A FIXED RADIAL DISTANCE FROM THE CENTER OF THE CYLINDER

	Uniform distribution of activity	Activity in a line source placed at 2.5 and 1.0 cm from the center of the two phantoms
Rat	19.1 %	18.0 %
Mouse	8.9 %	9.1 %

TABLE V
CALCULATED SCATTER FRACTION VALUES FROM SINOGRAMS OF MONTE CARLO SIMULATIONS FOR A LINE SOURCE RAT PHANTOM IN AN A-PET SCANNER. THE RESULTS ARE SHOWN FOR VARYING WINDOW WIDTHS UNDER THE SINOGRAM PROFILE PEAKS THAT ARE USED FOR ESTIMATING THE SCATTER

	Scatter Fraction (%)
From counting events in Monte Carlo	18.0
Using window width of 16 mm	16.5
Using window width of 14 mm	17.1
Using window width of 12 mm	18.4

and scatter properties similar to water. The activity in the two cylinders was localized in a line source of length similar to the cylinder length, with the line source placed in a hole drilled at radii of 2.5 and 1.0 cm from the center of the rat and mouse phantoms, respectively. The choice for the radial position of the line source in each cylinder was dictated by scanner Monte Carlo simulations performed to evaluate the line source position which gave a scatter fraction similar to that in a uniformly filled cylindrical phantom of the same size. Table IV summarizes the results obtained by a simple counting of the number of scatter and true coincidences for the different setups in the Monte Carlo simulations.

We produced sinograms for the different simulations and performed a scatter fraction analysis similar to the one prescribed in NU2-2001 standards for whole-body scanners. The sinograms were first rebinned into direct sinograms by using single-slice rebinning. In the NU2-2001 standards, the transverse FOV is restricted over the object by first setting all bins beyond a fixed radial distance (12 cm) to zero in each sinogram. For our initial evaluation of the simulation data, we used the complete animal scanner FOV of 12.8 cm. Within each sinogram and for each projection angle, the radial bin containing the maximum value was shifted so that radial bins with maximum value for all projections were aligned. A sum of these shifted projections was then used to produce a sinogram profile. A variable width window was placed around the peak of this profile to estimate true coincidences. In the NU2 standards, this window size is restricted to 4 cm based on the spatial resolution of whole-body PET scanners. The scatter within the peak was estimated by assuming a constant background under the peak, the level of which was determined by the average of the intensities near the edge of the peak (at $\pm 0.5 \times$ window width). Table V shows the scatter fraction results obtained for the rat line phantom for different window sizes as well as from counting the true and scattered events directly in the Monte Carlo. These results show that a window width of about 12 mm correctly predicts the scatter

TABLE VI
MEASURED SCATTER FRACTION VALUES FOR THE LYSO A-PET SCANNER

| LLD (keV) | Scatter Fraction (%) | |
	Rat line source phantom	Mouse line source phantom
250	25.9	10.2
385	17.8	10.0
410	14.4	9.8
430	12.8	8.9

fraction in the phantom. This window width, which is related to the spatial resolution of the scanner, is consistent with the 4-cm window width for a whole-body scanner if we consider the fact that there is about a factor of three improvement in spatial resolution in moving from a clinical whole-body scanner to a 2-mm resolution system.

For scanner measurements we acquired low count-rate data (random coincidence rate less than 1% of true coincidence rate) with the two line source phantoms (rat and mouse) filled with ^{18}F-FDG. Since LYSO contains a small percentage of radioactive ^{176}Lu, LYSO-based PET scanners have a nonzero random coincidence rate even without activity in the FOV. This effect has been studied recently to evaluate its impact on the measurement of scatter and background fractions for whole-body clinical PET scanners where the random coincidence rate never reaches levels as low as 1% of the true coincidence rate [50]. However, in an animal scanner the amount of LYSO used is small compared to a clinical whole-body scanner, and the requirement for random coincidences being less than 1% of the true coincidences can be achieved. Data analysis as described above was performed to produce the sinogram radial profiles. The FOV, however, was restricted over the object regions of 7.2 and 3.6 cm for the rat and mouse phantoms, respectively, and a window width of 12 mm (as determined above in Table V) was used to estimate the measured scatter fraction. These scatter measurements were performed as function of lower energy gate (LLD) for the LYSO scanner while keeping the upper gate fixed at 665 keV. The results are summarized in Table VI. For the default energy window (385–665 keV), the scatter fraction in the GSO scanner is 9.7% and 19.0% for the mouse and rat phantoms, respectively.

D. Count-Rate Performance

The same two phantoms (rat and mouse) as used above in the scatter fraction measurement were used with a high starting activity level (^{18}F-FDG) to measure the count-rate performance of the two systems. Data were dynamically acquired until almost all the activity had decayed away. Analysis similar to that used earlier for scatter fraction was performed to estimate the "background fraction." Background fraction is defined as $(Sc + R)/(T + Sc + R)$, where R are random coincidence counts. At low count-rates (random coincidences <1% of true coincidences), the background fraction is the same as the scatter fraction, while at higher count-rates, it is the fraction of total coincidence counts that are random and scatter coincidences.

If a constant scatter fraction (as determined from the low count-rate analysis) is assumed, the random coincidence rate
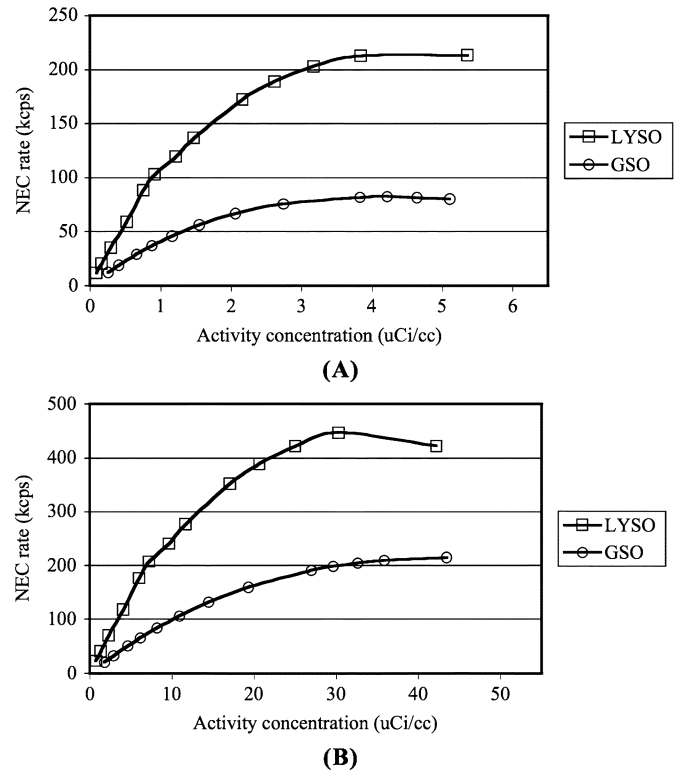

(A)

(B)

Fig. 3. NEC plots for the (A) rat and (B) mouse line phantoms in the two A-PET scanners. The coincidence timing window was 12 ns while the energy window was set at 385–665 keV.

can be determined from the background fraction values at higher activity levels. The noise equivalent count (NEC) rate is then calculated. The NEC rate is given by

$$NEC = \frac{T \times T}{T + Sc + kR}$$

where the true, scatter, and random counts are restricted to those that lie within the phantom FOV (circular regions of 7.2- and 3.6-cm-diameter for the two phantoms) and k is set to 1 or 2 depending on whether we use direct randoms subtraction or variance reduction techniques for estimating a smooth randoms distribution. In these calculations, we set $k = 1$ for a smooth randoms subtraction.

The value of the coincidence timing window 2τ was fixed at 12 ns for these measurements, and the energy window is 385–665 keV.

Fig. 3 shows the NEC plots for the GSO and LYSO scanners with the (A) rat and (B) mouse line phantoms. Note the significant NEC rate increase with the use of LYSO. The NEC peak for LYSO is due to saturation in the position calculating unit (PPU) in the electronics. In this plot, the coincidence timing window and energy window for the LYSO scanner were kept the same as in the GSO scanner. However, because of better timing characteristics of the LYSO scintillator, we also investigated reducing the coincidence timing window in the LYSO scanners. Our measurements with different coincidence timing windows for LYSO showed that by reducing the timing window to 7 ns, we can reduce random coincidences without reducing the scanner's sensitivity to true coincidences.
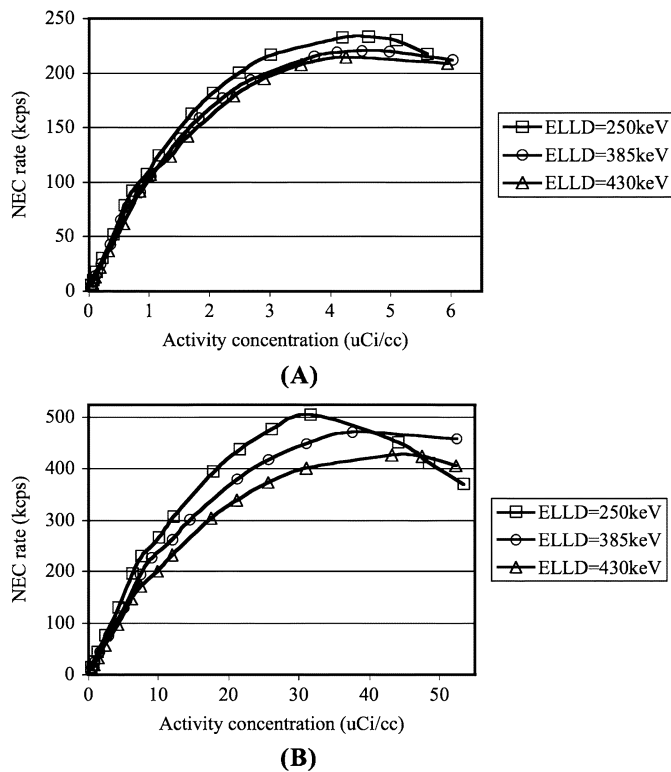
(A)

(B)

Fig. 4. NEC plots for the (A) rat and (B) mouse line phantoms in the LYSO A-PET scanner for a coincidence timing of 7 ns and varying energy windows. The upper level of the energy window was kept fixed at 665 keV while the lower level (LLD) was changed.

Fig. 4 shows the NEC rates for the LYSO A-PET scanner with a 7 ns coincidence timing window and different energy windows. In these measurements only the lower level of the energy window (LLD) was varied while the upper level was fixed at 665 keV. These results indicate that optimal results (highest peak NEC) are obtained by using a 7 ns coincidence timing window and setting the lower level of the energy window at 250 keV. The increased sensitivity of the scanner with LLD set at 250 keV compensates for the increase in scatter fraction, resulting in a higher NEC rate at low activity levels. At higher activity levels, the lower LLD is less of an advantage due to a higher random coincidence rate. However, this effect becomes noticeable only at high rates at which the PPU saturation starts to dominate. The true, scatter, and random coincidence rates for this setting (LLD set at 250 keV) are shown in Fig. 5.

E. Image Quality

A small Data Spectrum Micro Deluxe phantom (4.5 cm in diameter by 3.7 cm in length) with a cold rod insert was imaged. The rods are grouped into sectors with diameters of 1.2, 1.6, 2.4, 3.2, 4.0, and 4.8 mm, and the center-to-center rod spacing is twice the rod diameter. The data were reconstructed with 3D-RAMLA into cubic voxels of dimension 0.5 mm. The fully corrected image from the LYSO scanner for a 15 min scan time is shown in Fig. 6. The 1.6-mm rods are easily distinguishable.

For contrast recovery measurement in the LYSO scanner, we used a 7.6-cm-diameter by 5.0-cm-length cylinder containing a fillable sphere within to help predict tumor quantification. Measurements were performed with an activity concentration ratio of 8:1 in the sphere with respect to the cylinder background
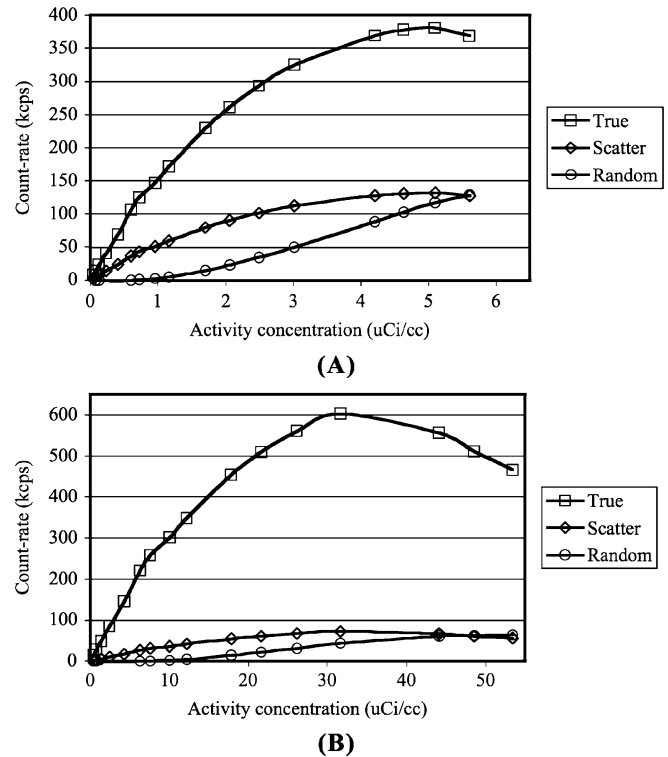

(A)

(B)

Fig. 5. True, scatter, and random coincidence rates for the (A) rat and (B) mouse line phantoms in the LYSO for a coincidence timing window of 7 ns and an energy window of 250–665 keV.
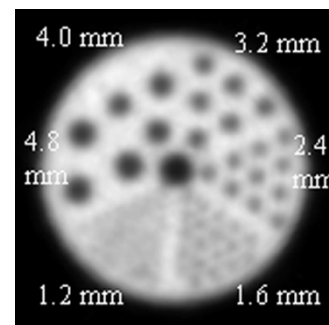

Fig. 6. Image of the Micro Deluxe phantom with the cold rod insert from the LYSO scanner. The rod diameters for each sector are marked.

and a total activity of about 1.2 mCi inside the FOV. Measurements were made for two different spheres (1.4- and 0.8-cm diameter). Data were collected for 15 min and image reconstruction performed using both 3D-FRP and 3D-RAMLA. The count density was determined for circular regions of interest (ROIs) drawn with varying size diameter (D) in the central slice over the hot sphere as well as the background. As described in the NU 2-2001 contrast measurement, the percent contrast (CRC) for the hot sphere was defined as

$$\text{CRC} = 100\% \times \frac{\left(\frac{C_H}{C_B} - 1\right)}{\left(\frac{a_H}{a_B} - 1\right)}$$

where C_H is the count density in the ROI for the sphere, C_B is the average count density of the background, and a_H and a_B are the activity concentrations in the spheres and background (8 and 1), respectively. In Table VII, we summarize the CRC

TABLE VII
CONTRAST RECOVERY (CRC) VALUES OBTAINED WITH 8-mm AND 14-mm DIAMETER SPHERES IN A WARM BACKGROUND (ACTIVITY UPTAKE RATIO OF 8:1). THE RECOVERY IS ABOUT 80% WHEN DRAWING ROI ABOUT HALF THE PHYSICAL DIAMETER OF THE SPHERES

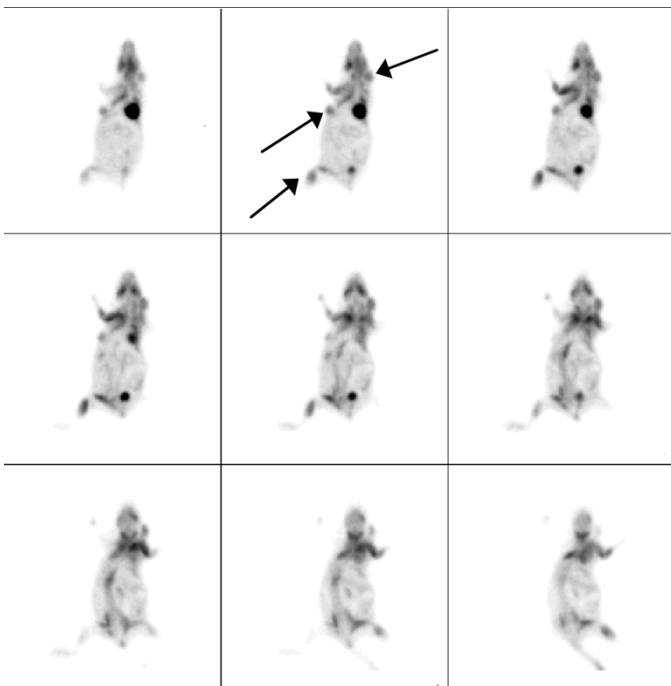| ROI diameter in units	CRC (%)	
of sphere diameter	14 mm sphere	8 mm sphere
0.25	85	78
0.50	84	75
1.00	68	62

Fig. 7. An FDG study of a mouse with multiple tumors, imaged on the LYSO scanner. The arrows indicate the presence of tumors.

values versus the ROI size for images reconstructed with 3D-RAMLA. The CRC is about 80% when ROIs less than half the physical diameter of the two spheres are used. The results with 3D-FRP reconstruction were similar.

F. Animal Studies

The animal scanner has been in routine use for animal studies since June 2003, first with GSO for six months, and since December 2003 with LYSO. Images are qualitatively improved with LYSO due to improved sensitivity and higher NEC values. The injected activity is typically about 0.5 mCi, where the dose is limited by the volume we can inject (0.2 μL for mice). A representative ^{18}F-FDG study of a mouse with multiple tumors imaged on the LYSO system is shown in Fig. 7 The mouse was injected with 0.4 mCi of ^{18}F-FDG two hours before imaging and scanned for a total of 15 min in a single bed position. The total collected events were 86 million and the image was reconstructed in cubic voxels of dimension 0.5 mm using 3D-RAMLA.

Fig. 8(A) shows a ^{11}C-raclopride study for a cat injected with 1.0 mCi of activity while Fig. 8(B) shows a ^{11}C-raclopride study for a mouse injected with 0.14 mCi of activity. Raclopride binds to the dopamine D2 receptors. It is important to be able to identify the striatum region in the brain that contains D2 receptors to
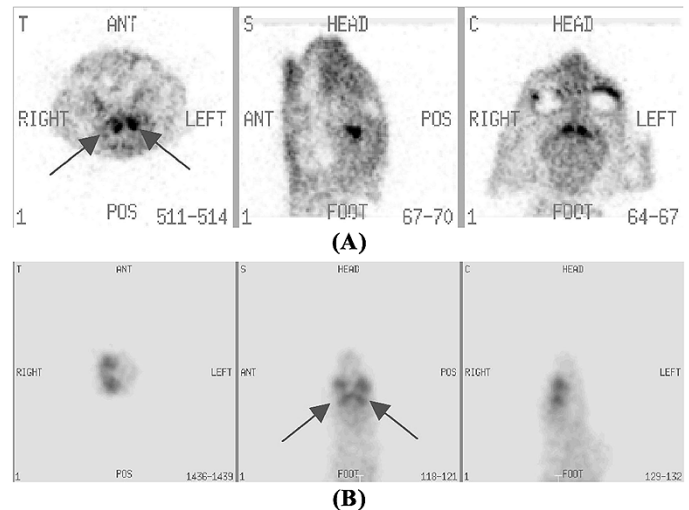

Fig. 8. ^{11}C-raclopride study on (A) cat and (B) mouse acquired on the LYSO A-PET scanner. The arrows indicate the clear delineation of the striatum region in the two animals.

determine the biodistribution of raclopride. The striatum region is well distinguished in both these images which are summed over dynamic frames acquired for one hour and which are used for defining the ROIs used to generate the time activity curves. The start collect rates (first frame) were 15 and 30 kcps for the cat and mouse, respectively, leading to a high count density per voxel and accurate quantitation for generating the time activity plots.

IV. DISCUSSION AND CONCLUSIONS

Compared to our experience with human PET scanners, the animal scanner presented some additional challenges. Not only does the reduction in crystal cross-section to 2×2 mm^2 reduce the light output relative to 4×4 mm^2 or larger crystal but in addition the 19-mm-diameter PMTs have a smaller fraction of the total area covered by the photocathode in comparison to 39 or 50-mm-diameter PMTs used in human scanners. This leads to poorer crystal identification and energy resolution compared to human scanners using GSO. In addition, the lower price of GSO relative to LYSO could not easily be translated into either thicker crystals or longer axial FOV (as is possible in human scanners), since we were unwilling to give up spatial resolution as result of using longer crystals. A larger axial FOV would bring little additional benefit once the axial FOV exceeds the size of the animal. This is in contrast to human scanners, where it is possible to compensate for lower stopping power crystals by increasing the axial FOV of the scanner. Our use of LYSO with a higher stopping power helps overcome this obstacle. The sensitivity of the animal scanner for the line source increased by almost a factor of two after switching the scintillator from GSO to LYSO. A larger increase in sensitivity was observed for the measurements with the point source.

The spatial resolution in the LYSO scanner is slightly better than that measured for the GSO version and is more noticeable at the FWTM level. This improvement in spatial resolution can be explained by two effects: 1) individual crystal identification in a flood map (see Fig. 1 for LYSO) was more difficult, with GSO leading to some mispositioning of events, and 2) the higher

effective Z value of LYSO compared to GSO. A high-Z scintillator results in a larger fraction of photoelectric events compared to Compton scatter, thereby reducing the tails in the point spread function. Using a narrow profile with the LYSO scanner, we notice that the localized spatial resolution is better. However, the measurement with a narrow profile is less robust and more susceptible to fluctuations in count density and may not always represent the achievable spatial resolution in the scanner, especially when analyzing 3-D reconstructed images.

For the scatter fraction and count-rate analysis, we developed phantoms of sizes comparable to a rat and a mouse and modified the analysis procedure from the NEMA NU2-2001 standards for estimating the scatter fraction in mice and rats. Our results show that the expected scatter fraction is small and does not increase very fast as a function of LLD for mouse-sized objects.

From the count-rate data for the same energy and coincidence timing window, we see that the high sensitivity of the LYSO scanner leads to more than a factor of two increase in the NEC rate over the GSO scanner (see Fig. 3). The LYSO NEC peak is due to saturation in the PPU in the electronics. Mouse and rat studies with ^{18}F and ^{11}C tracers are performed at low activity levels of less than 0.5 mCi, corresponding to less than 10 and 1 μCi/cc in a mouse and rat, respectively. As seen in Fig. 4, this is well below the saturation limit and is not a limiting factor. In the future, if animal studies dictate such high activity levels, the PPU can be upgraded to handle higher data rates. Our results with the different energy windows show that there is some improvement in the NEC rate when a 250–665 keV energy window is used due to the increased sensitivity.

The data from the Micro Deluxe phantom indicate the good image quality achieved due to high resolution, high sensitivity, and accurate data correction characteristics of the A-PET scanner and is borne out in the sample animal studies shown above. Additionally, the high contrast recovery achieved by this scanner, as shown in the CRC values for the hot sphere, indicate the capability to produce accurate, quantitative data from this scanner.

REFERENCES

[1] R. Lecomte, J. Cadorette, S. Rodrigue, D. Lapointe, D. Rouleau, M. Bentourkia, R. Yao, and P. Msaki, "Initial results from the Sherbrooke avalanche photodiode positron tomograph," *IEEE Trans. Nucl. Sci.*, vol. 43, no. 3, pp. 1952–1957, Jun. 1996.

[2] A. F. Chatziioannou, S. R. Cherry, Y. P. Shao, R. W. Silverman, K. Meadors, T. H. Farquhar, M. Pedarsani, and M. E. Phelps, "Performance evaluation of microPET: A high-resolution lutetium oxyorthosilicate PET scanner for animal imaging," *J. Nucl. Med.*, vol. 40, pp. 1164–1175, 1999.

[3] S. R. Cherry, Y. Shao, R. W. Silverman, K. Meadors, S. Siegel, A. Chatziioannou, J. W. Young, W. F. Jones, J. C. Moyers, D. Newport, A. Boutefnouchet, T. H. Farquhar, M. Andreaco, M. J. Paulus, D. M. Binkley, R. Nutt, and M. E. Phelps, "Micropet—A high-resolution PET scanner for imaging small animals," *IEEE Trans. Nucl. Sci.*, vol. 44, no. 3, pp. 1161–1166, Jun. 1997.

[4] Y. C. Tai, A. Chatziioannou, S. Siegel, J. Young, D. Newport, R. N. Goble, R. E. Nutt, and S. R. Cherry, "Performance evaluation of the microPET P4: A PET system dedicated to animal imaging," *Phys. Med. Biol.*, vol. 46, pp. 1845–1862, 2001.

[5] Y. C. Tai, A. F. Chatziioannou, Y. F. Yang, R. W. Silverman, K. Meadors, S. Siegel, D. F. Newport, J. R. Stickel, and S. R. Cherry, "MicroPET II: Design, development, and initial performance of an improved microPET scanner for small-animal imaging," *Phys. Med. Biol.*, vol. 48, pp. 1519–1537, 2003.

[6] Y. C. Tai, A. Ruangma, R. Laforest, S. Siegel, and D. F. Newport, "Performance evaluation of the microPET (R) Focus: A second generation small animal PET system.," *J. Nucl. Med.*, vol. 44, pp. 159p–160p, 2003.

[7] C. Knoess, S. Siegel, A. Smith, D. Newport, R. Richerzhagen, A. Winkeler, A. Jacobs, R. N. Goble, R. Graf, K. Wienhard, and W. D. Heiss, "Performance evaluation of the microPET R4 PET scanner for rodents," *Eur. J. Nucl. Med.*, vol. 30, pp. 737–747, 2003.

[8] A. P. Jeavons, R. A. Chandler, and C. A. R. Dettmar, "A 3D HIDAC-PET camera with sub-millimeter resolution for imaging small animals," *IEEE Trans. Nucl. Sci.*, vol. 46, no. 3, pp. 468–473, Jun. 1999.

[9] S. I. Ziegler, B. J. Pichler, G. Boening, M. Rafecas, W. Pimpl, E. Lorenz, N. Schmitz, and M. Schwaiger, "A prototype high-resolution animal positron tomograph with avalanche photodiode arrays and LSO crystals," *Eur. J. Nucl. Med.*, vol. 28, pp. 136–143, 2001.

[10] S. Siegel, J. J. Vaquero, L. Aloj, J. Seidel, E. Jagoda, W. R. Gandler, W. C. Eckelman, and M. V. Green, "Initial results from a PET planar small animal imaging system," *IEEE Trans. Nucl. Sci.*, vol. 46, no. 3, pp. 571–575, Jun. 1999.

[11] J. A. Correia, C. A. Burnham, D. Kaufman, A. L. Brownell, and A. J. Fischman, "Performance evaluation of MMP-II: A second-generation small animal PET," *IEEE Trans. Nucl. Sci.*, vol. 51, no. 1, pp. 21–26, Feb. 2004.

[12] P. M. Bloomfield, R. Myers, S. P. Hume, T. J. Spinks, A. A. Lammertsma, and T. Jones, "Three-dimensional performance of a small-diameter positron emission tomograph," *Phys. Med. Biol.*, vol. 42, pp. 389–400, 1997.

[13] I. Y. Chen, J. C. Wu, J. J. Min, G. Sundaresan, X. Lewis, Q. W. Liang, H. R. Herschman, and S. S. Gambhir, "Micro-positron emission tomography imaging of cardiac gene expression in rats using bicistronic adenoviral vector-mediated gene delivery," *Circulation*, vol. 109, pp. 1415–1420, 2004.

[14] J. J. Min, M. Iyer, and S. S. Gambhir, "Comparison of [F-18]FHBG and [C-14]FIAU for imaging of HSV1-tk reporter gene expression: Adenoviral infection vs stable transfection," *Eur. J. Nucl. Med.*, vol. 30, pp. 1547–1560, 2003.

[15] S. S. Gambhir, "Molecular imaging of cancer with positron emission tomography," *Nat. Rev. Cancer*, vol. 2, pp. 683–693, 2002.

[16] D. H. S. Silverman, G. W. Small, C. Y. Chang, C. S. Lu, M. A. K. de Aburto, W. Chen, J. Czernin, S. I. Rapoport, P. Pietrini, G. E. Alexander, M. B. Schapiro, W. J. Jagust, J. M. Hoffman, K. A. Welsh-Bohmer, A. Alavi, C. M. Clark, E. Salmon, M. J. de Leon, R. Mielke, J. L. Cummings, A. P. Kowell, S. S. Gambhir, C. K. Hoh, and M. E. Phelps, "Positron emission tomography in evaluation of dementia—Regional brain metabolism and long-term outcome," *J. Am. Med. Assoc.*, vol. 286, pp. 2120–2127, 2001.

[17] S. S. Gambhir, H. R. Herschman, S. R. Cherry, J. R. Barrio, N. Satyamurthy, T. Toyokuni, M. E. Phelps, S. M. Larson, J. Balatoni, R. Finn, M. Sadelain, J. Tjuvajev, and R. Blasberg, "Imaging transgene expression with radionuclide imaging technologies," *Neoplasia*, vol. 2, pp. 118–138, 2000.

[18] S. P. Hume and T. Jones, "Positron emission tomography (PET) methodology for small animals and its application in radiopharmaceutical preclinical investigation," *Nucl. Med. Biol.*, vol. 25, pp. 729–732, 1999.

[19] S. P. Hume, R. N. Gunn, and T. Jones, "Pharmacological constraints associated with positron emission tomographic scanning of small laboratory animals," *Eur. J. Nucl. Med.*, vol. 25, pp. 173–176, 1998.

[20] M. E. Phelps, "PET: The merging of biology and imaging into molecular imaging," *J. Nucl. Med.*, vol. 41, pp. 661–681, 2000.

[21] H. I. Kornblum, D. M. Araujo, A. J. Annala, K. J. Tatsukawa, M. E. Phelps, and S. R. Cherry, "*In vivo* imaging of neuronal activation and plasticity in the rat brain by high resolution positron emission tomography (microPET)," *Nat. Biotech.*, vol. 18, pp. 655–660, 2000.

[22] S. S. Gambhir, J. R. Barrio, L. Wu, M. Iyer, M. Namavari, N. Satya-murthy, E. Bauer, C. Parrish, D. C. MacLaren, A. R. Borghei, L. A. Green, S. Sharfstein, A. J. Berk, S. R. Cherry, M. E. Phelps, and H. R. Herschman, "Imaging of adenoviral-directed herpes simplex virus type 1 thymidine kinase reporter gene expression in mice with radiolabeled ganciclovir," *J. Nucl. Med.*, vol. 39, pp. 2003–2011, 1998.

[23] S. S. Gambhir, J. R. Barrio, M. E. Phelps, M. Iyer, M. Namavari, N. Satyamurthy, L. Wu, L. A. Green, E. Bauer, D. C. MacLaren, K. Nguyen, A. J. Berk, S. R. Cherry, and H. R. Herschman, "Imaging adenoviral-directed reporter gene expression in living animals with positron emission tomography," *Proc. Nat. Acad. Sci. (USA)*, vol. 96, pp. 2333–2338, 1999.

[24] H. R. Herschman, D. C. MacLaren, M. Iyer, M. Namavari, K. Bobinski, L. A. Green, L. Wu, A. J. Berk, T. Toyokuni, J. R. Barrio, S. R. Cherry, M. E. Phelps, E. P. Sandgren, and S. S. Gambhir, "Seeing is believing: Non-invasive, quantitative, and repetitive imaging of reporter gene expression in living animals, using positron emission tomography," *J. Neurosci. Res.*, vol. 59, pp. 699–705, 2000.

[25] D. C. MacLaren, T. Toyokuni, S. R. Cherry, J. R. Barrio, M. E. Phelps, H. R. Herschman, and S. S. Gambhir, "PET imaging of transgene expression," *Biological Psy.*, vol. 48, pp. 337–348, 2000.

[26] S. P. Hume, D. J. Brown, E. Ashworth, E. Hirani, S. K. Luthra, and A. A. Lammertsma, "*In-vivo* saturation kinetics of 2 dopamine transporter probes measured using a small animal positron-emission-tomography scanner," *J. Neurosci. Meth.*, vol. 76, pp. 45–51, 1997.

[27] E. Hirani, J. Opacka-Juffry, R. Gunn, I. Khan, T. Sharp, and S. Hume, "Pindolol occupancy of 5-HT1A receptors measured *in vivo* using small animal positron emission tomography with carbon-11 labeled WAY 100 635," *Synapse*, vol. 36, pp. 330–341, 2000.

[28] S. Surti, J. S. Karp, A. E. Perkins, R. Freifelder, and G. Muehllehner, "Design evaluation of A-PET: A high sensitivity animal PET camera," *IEEE Trans. Nucl. Sci.*, vol. 50, no. 5, pp. 1357–1363, Oct. 2003.

[29] S. Surti, J. S. Karp, R. Freifelder, and F. Liu, "Optimizing the performance of a PET detector using discrete GSO crystals on a continuous lightguide," *IEEE Trans. Nucl. Sci.*, vol. 47, no. 3, pp. 1030–1036, Jun. 2000.

[30] R. Lecomte, J. Cadorette, P. Richard, S. Rodrigue, and D. Rouleau, "Design and engineering aspects of a high-resolution positron tomograph for small animal imaging," *IEEE Trans. Nucl. Sci.*, vol. 41, no. 4, pp. 1446–1452, Aug. 1994.

[31] S. I. Ziegler, B. J. Pichler, G. Boening, H. Rafecas, S. Bieler, W. Pimpl, E. Lorenz, and M. Schwaiger, "MadPET: High resolution animal pet with avalanche photodiode arrays and LSO crystals," *J. Nucl. Med.*, vol. 41, pp. 20p–20p, 2000.

[32] J. S. Karp, S. Surti, M. E. Daube-Witherspoon, R. Freifelder, C. A. Cardi, L. E. Adam, K. Bilger, and G. Muehllehner, "Performance of a brain PET camera based on anger-logic gadolinium oxyrorthosilicate detectors," *J. Nucl. Med.*, vol. 44, pp. 1340–1349, 2003.

[33] S. Surti and J. S. Karp, "Imaging characteristics of a 3-dimensional GSO whole-body PET camera," *J. Nucl. Med.*, vol. 45, pp. 1040–1049, 2004.

[34] J. S. Karp, G. Muehllehner, D. Beerbohm, and D. Mankoff, "Event localization in a continuous scintillation detector using digital processing," *IEEE Trans. Nucl. Sci.*, vol. NS-33, pp. 550–555, 1986.

[35] J. S. Karp, G. Muehllehner, D. A. Mankoff, C. E. Ordonez, J. M. Ollinger, M. E. Daube-Witherspoon, A. T. Haigh, and D. J. Beerbohm, "Continuous-slice PENN-PET: A positron tomograph with volume imaging capability," *J. Nucl. Med.*, vol. 31, pp. 617–627, 1990.

[36] D. A. Mankoff, G. Muehllehner, and G. E. Miles, "A local coincidence triggering system for PET tomographs composed of large-area position-sensitive detectors," *IEEE Trans. Nucl. Sci.*, vol. 37, no. 2, pp. 730–736, Apr. 1990.

[37] R. Accorsi, L.-E. Adam, and J. S. Karp, "Implementation of a single scatter simulation algorithm for 3D PET: Application to emission and transmission," in *Proc. 2002 IEEE Nuclear Science Symp. Medical Imaging Conf. Rec.*, S. Metzler, Ed., Piscataway, NJ, 2003, pp. M3–186.

[38] M. E. Casey and E. J. Hoffman, "Quantitation in positron emission computed tomography: 7. A technique to reduce noise in accidental coincidence measurements and coincidence efficiency calibration," *J. Comput. Assist. Tomogr.*, vol. 10, pp. 845–850, 1986.

[39] M. E. Daube-Witherspoon, L. M. Popescu, S. Matej, C. A. Cardi, R. M. Lewitt, and J. S. Karp, "Rebinning and reconstruction of point source transmission data for positron emission tomography," presented at the IEEE Nuclear Science Symp. Medical Imaging Conf., Portland, OR, 2003.

[40] K. Lange and R. Carson, "EM reconstruction algorithms for emission and transmission tomography," *J. Comput. Assist. Tomogr.*, vol. 8, pp. 306–316, 1984.

[41] S. H. Manglos, G. M. Gagne, A. Krol, F. D. Thomas, and R. Narayanaswamy, "Transmission maximum-likelihood reconstruction with ordered subsets for cone-beam Ct," *Phys. Med. Biol.*, vol. 40, pp. 1225–1241, 1995.

[42] J. A. Browne and A. R. DePierro, "A row-action alternative to the EM algorithm for maximizing likelihoods in emission tomography," *IEEE Trans. Med. Imag.*, vol. 15, pp. 687–699, 1996.

[43] M. E. Daube-Witherspoon, S. Matej, J. S. Karp, and R. M. Lewitt, "Application of the row action maximum likelihood algorithm with spherical basis functions to clinical PET imaging," *IEEE Trans. Nucl. Sci.*, vol. 48, no. 1, pp. 24–30, Feb. 2001.

[44] A. R. DePierro, "On some nonlinear iterative relaxation methods in remote sensing," *Matematica Aplicada Computacional*, vol. 8, pp. 153–166, 1989.

[45] D. L. Bailey, T. Jones, and T. S. Spinks, "A method for measuring the absolute sensitivity of positron emission tomographic scanners," *Eur. J. Nucl. Med.*, vol. 18, pp. 374–379, 1991.

[46] M. E. Daube-Witherspoon, J. S. Karp, M. E. Casey, F. P. DiFilippo, H. Hines, G. Muehllehner, V. Simcic, C. W. Stearns, L.-E. Adam, S. Kohlmyer, and V. Sossi, "PET performance measurements using the NEMA NU 2-2001 standard," *J. Nucl. Med.*, vol. 43, pp. 1398–1409, 2002.

[47] *Performance Measurements of Positron Emission Tomographs*, NU 2-2001, 2001.

[48] S. Matej and R. M. Lewitt, "3D-FRP: Direct fourier reconstruction with Fourier reprojection for fully 3-D PET," *IEEE Trans. Nucl. Sci.*, vol. 48, no. 4, pp. 1378–1385, Aug. 2001.

[49] M. Defrise, P. E. Kinahan, D. W. Townsend, C. Michel, M. Sibomana, and D. F. Newport, "Exact and approximate rebinning algorithms for 3D PET data," *IEEE Trans. Med. Imag.*, vol. 11, no. 2, pp. 145–158, Apr. 1997.

[50] C. C. Watson, M. E. Casey, L. Eriksson, T. Mulnix, D. Adams, and B. Bendriem, "NEMA NU 2 performance tests for scanners with intrinsic radioactivity," *J. Nucl. Med.*, vol. 45, pp. 822–826, 2004.